Published in final edited form as:
Biomaterials. 2011 October ; 32(30): 7491–7502. doi:10.1016/j.biomaterials.2011.06.032.

Osteoconductive Protamine-based Polyelectrolyte Multilayer Functionalized Surfaces

Raymond E. Samuel[1,3], **Anita Shukla**[1,3], **Daniel H. Paik**[1], **Mary X. Wang**[1], **Jean C. Fang**[1], **Daniel J. Schmidt**[1], and **Paula T. Hammond**[1,2]

Paula T. Hammond: hammond@mit.edu

[1]Department of Chemical Engineering, Massachusetts Institute of Technology, 77 Massachusetts Avenue, Cambridge, MA 02139 (USA)

[2]David H. Koch Institute for Integrative Cancer Research, Massachusetts Institute of Technology, 77 Massachusetts Avenue, Cambridge, MA 02139 (USA)

Abstract

The integration of orthopedic implants with host bone presents a major challenge in joint arthroplasty, spinal fusion and tumor reconstruction. The cellular microenvironment can be programmed via implant surface functionalization allowing direct modulation of osteoblast adhesion, proliferation, and differentiation at the implant-bone interface. The development of layer-by-layer assembled polyelectrolyte multilayer (PEM) architectures has greatly expanded our ability to fabricate intricate nanometer to micron scale thin film coatings that conform to complex implant geometries. The in vivo therapeutic efficacy of thin PEM implant coatings for numerous biomedical applications has previously been reported. We have fabricated protamine-based PEM thin films that support the long-term proliferation and differentiation of pre-osteoblast cells on non-cross-linked film coated surfaces. These hydrophilic PEM functionalized surfaces with nanometer-scale roughness facilitated increased deposition of calcified matrix by osteoblasts in vitro, and thus offer the potential to enhance implant integration with host bone. The coatings can make an immediate impact in the osteogenic culture of stem cells and assessment of the osteogenic potential of new therapeutic factors.

1. Introduction

Stable integration of biomedical implants with host tissue is critical for the success of numerous surgical procedures in orthopedics, dentistry, plastic surgery, and neurosurgery [1, 2]. The great challenge is to enhance host cell/extracellular matrix interactions at the interface with metallic, ceramic, synthetic or natural polymeric surgical implants. Implant surface coatings have emerged as a means of modulating cellular events at the implant-tissue interface [3, 4]. The use of high temperatures in conventional implant coating methods (plasma spraying and laser ablation) is generally incompatible with production of surface

Correspondence to: Paula T. Hammond, hammond@mit.edu.

[3]R.E.S. and A.S. contributed equally to this work.

Conflict of Interest

The aurthors confirm that there are no conflicts of interest associated with this publication.

coatings containing active biological agents [5, 6]. Layer-by-layer (LbL) thin film assembly is an inexpensive, aqueous, conformal coating technique that can be used to efficiently coat surgical implants with biological agents that greatly enhance implant integration with host tissue [7, 8].

LbL assembly of polyelectrolyte multilayer (PEM) thin film coatings is driven by the alternating deposition of polymers with complementary electrostatic functionalities [9, 10]. The LbL assembly process produces nanometer to micron scale thin film coatings. It is anticipated that LbL film surface functionalization of biomedical devices will be a technological approach that is readily translatable to true clinical applications [11, 12]. Attaining adequate adhesion, proliferation, differentiation, and sustained survival of cells on these nano-layered surface coatings are some of the major obstacles that must be overcome for successful use of PEMs in drug delivery, device integration, and tissue engineering applications. In order for these biomaterials to attain their full potential, innovative methods must be employed to improve the cellular compatibility of PEM-coated devices and to direct specific cellular responses with these functionalized implant surfaces.

A major benefit of LbL assembly is the potential to achieve controlled and sequential delivery of therapeutic agents by tuning the deposition of these agents at specific layers within the film [13–15]. It has previously been demonstrated that conformal coatings of substrates with certain PEM architectures containing one or more therapeutic agents (e.g. nucleic acids, proteins, nanoparticles, and small molecule drugs), can be used to achieve prolonged, controlled release of the therapeutic(s) with controlled top-down erosion of the PEM [16, 17]. However, it is not always straightforward to achieve good cell adhesion on these therapeutic- loaded thin films, depending on the thickness, charge and mechanical properties of the film, and post-fabrication cross-linking methods can sometimes compromise the de novo incorporation of biological therapeutics within the architecture of these PEMs, or change desired release kinetics [18, 19]. For these reasons, there is a strong impetus to understand the cell-material interface of layer-by-layer thin films and generate alternative means of manipulating those interactions.

It is well established that cellular interactions with PEMs are highly influenced by the biomechanical properties of the thin film [20, 21]. Rubner and co-workers' pioneering studies on the design of cytophilic and cytophobic PEMs demonstrated that the selection of polyelectrolytes used in PEM fabrication governs the mechanical stiffness and resultant cellular adhesion to PEM coated surfaces [22–24]. A common means of improving cellular adhesion to PEMs has been to increase the mechanical strength of the PEM via post-fabrication cross-linking of the polyelectrolyte components within the multilayer films [20, 25]. These post-fabrication processes typically utilize chemicals, UV irradiation, or thermal cross-linking to achieve an increase in the mechanical integrity of the multilayer films [26, 27]. These methods may potentially modify therapeutic cargo embedded in the film during its initial fabrication, mitigating or disrupting the biological activity of these films. Furthermore, there are several applications of interest, from orthopedic implant devices to bone and cartilage tissue engineering applications, in which multilayer thin film platforms designed for enhanced osteointegration are particularly desirable.

Researchers are actively involved in developing methods to facilitate the use of PEMs for the delivery of osteoinductive factors (growth factors and vectors harboring transgenes) from the surface of orthopedic implants. In contrast to the use of organic osteoinductive agents, the application of osteoconductive materials to the surface of orthopedic implants has primarily focused on the use of inorganic crystalline (calcium phosphate and hydroxyapatite) or ceramic materials. Few studies have explored the use of organic polymers as osteoconductive coatings for orthopedic implant surfaces. Protamine sulfate

(PrS) is a natural polyamine that facilitates the condensation of DNA in sperm and plays a pivotal role during fertilization [28]. It is an FDA approved polypeptide used for the clinical reversal of heparin overdose (excessive bleeding disorder) and is also a component in a widely used insulin formulation [29]. The protamine used in these studies was isolated from herring sperm; 21 of its 32 amino acids are the cationic amino acid arginine (Fig. 1). Thus, the high net positive charge (+21) of protamine at physiologic pH is the basis for its popularity for use in augmenting in vitro transfection of plasmid DNA vectors into mammalian cells [30]. Protamine is also a popular polycation for the electrostatic coating of nanoparticles and multilayer films used in drug delivery [31–33]. Herein, we have developed and characterized protamine-based LbL PEM surface coatings for their ability to support osteoblast function in vitro.

2. Experimental

Materials

Protamine sulfate (PrS; MW = 4,500 Da), poly(sodium 4-styrenesulfonate) (SPS; MW = 70,000 Da), and tetrazolium [3-(4,5-dimethylthiazol-2-yl)-2,5-diphenyltetrazolium bromide] (MTT) were purchased from Sigma-Aldrich (St. Louis, MO). Alpha-minimum essential medium (α-MEM), fetal bovine serum (FBS), antibiotic-antimycotic solution, trypsin-EDTA, Hoechst 33242, and the Live/Dead® Viability/Cytotoxicity Kit for mammalian cells (L3342) were obtained from Invitrogen (Carlsbad, CA). Sodium acetate solution was purchased from Lonza (Portland, ME). Test grade n-type silicon wafers, quartz slides, and glass slides were obtained from Silicon Quest (Santa Clara, CA), Chemglass (Vineland, NJ), and VWR International (West Chester, PA), respectively. Deionized water (18.2 M Ω, Milli-Q Ultrapure Water System, Millipore) was utilized in all experiments.

Fabrication of PEM

LbL film assembly was performed using an automated slide stainer as previously described [34]. In brief, the substrate (silicon, quartz, or glass) was cleaned sequentially in methanol, ethanol, methanol and water, dried with filtered nitrogen, plasma etched for 5 minutes at high RF setting, and then immediately immersed in the polycationic PrS solution (2 mg/ml in 0.1 M sodium acetate buffer, pH 5.2) for at least 15 minutes prior to commencing the automated dipping protocol. The LbL protocol was designed to produce a bilayer PEM architecture through the alternating immersion of the substrate in the polycation (PrS) solution, two water rinses, the polyanion solution (SPS; 20 mM with respect to the polymer repeat unit), and two additional rinses of water [35]. This dipping protocol was repeated *n* times to produce the final PEM designated $(PrS/SPS)_n$, where n represents the number of bilayers deposited (Fig. 1). Upon fabrication the PEMs were dried with filtered nitrogen and stored in sealed vials at room temperature.

Dry Characterization of $(PrS/SPS)_n$ PEMs

Atomic force microscopy (AFM) imaging of the surface morphology of dry $(PrS/SPS)_n$ PEMs at n = 20, 40, 60, 80, 100, 180, 200, and 240 bilayers was conducted. A MultiMode 8 scanning probe microscope with a Nanoscope V controller from Veeco Metrology (Santa Barbara, CA) operated in Peak Force Tapping mode was utilized for all measurements. ScanAsyst software (Veeco) was used to map film height. Film morphology was tracked using silicon probes over a 10 μm × 10 μm area. Film root mean squared (RMS) roughness values were determined using NanoScope Analysis 1.10 software (Veeco). The thickness of dry $(PrS/SPS)_n$ PEMs were determined using a Tencor P16 profilometer as previously reported, with stylus force of 2 mg and scan length of 1 mm.

UV-Vis spectroscopy was used to determine the accumulation of PrS (amide bond at 200 nm and aromatic ring at 280 nm) and SPS (226 nm) during the PEM growth process. UV-Vis spectra were obtained from PEMs fabricated on quartz substrates using a VarianCary 6000i UV-Vis-NIR spectrophotometer. Circular dichroism (CD) was performed on dry PEMs fabricated on quartz substrates in order to determine whether the secondary structure of PrS was altered during film incorporation using an Aviv Biomedical 202 Circular Dichroism Spectrophotometer. Scan ranges spanned 300 nm to 170 nm. Difference spectra were obtained by subtracting baseline corrected (uncoated quartz slide) spectra of dry $(PrS/SPS)_n$ thin films oriented 90° relative to each other.

Liquid Phase Characterization of PEMs

Quartz Crystal Microbalance with Dissipation (QCM-D) was used to monitor the in situ deposition of the polyelectrolytes (PrS and SPS) on SiO_2 coated QCM-D quartz cystals. The resonance frequencies (overtones) of the crystals were monitored on a D300 QCM-D (Q-Sense, Inc.). The absolute resonance frequency (f) and the absolute dissipation (D) of at least four overtones were measured during the 10 minute flow period for the polycation solution, the Milli-Q water rinse, the polyanion solution, and the final Milli-Q water rinse of each deposited bilayer. All measurements were acquired at 25°C. Data was analyzed with aid of Q-Tools software (Q-Sense, Inc.).

Dynamic air-water contact angle measurements of $(PrS/SPS)_n$ PEMs were obtained using the sessile drop method on a Rame-Hart Contact Angle Goniometer. Advancing and receeding contact angles were measured after depositing 4 μl of MilliQ water to the surface. Spectroscopic ellipsometry (Woollam WVASE Spectroscopic Ellipsometer) was used to study the in situ swelling response of the PEMs. PEM thicknesses were measured in the dry state and after hydration in phosphate buffered saline, pH 7.2 without calcium and magnesium. All thickness measurements were obtained at room temperature with the light source at a 70° angle of incidence. The PEM thickness was determined by fitting the spectra with a Cauchy dispersion model.

The estimated Young's moduli of hydrated 20, 40, 60, and 80 bilayer PEMs were obtained in a fluid AFM cell on the Veeco AFM described earlier. The PEMs were hydrated in approximately 100 μL of 0.01 M PBS, pH 7.2 for all measurements. $(PrS/SPS)_n$ PEM moduli were tracked over a 10 μm × 10 μm area using silicon nitride probes in solution. The PeakForce Quantitative Nano-mechanical Property Mapping (PeakForce QNM) capabilities from Veeco were used to estimate the Young's moduli. The NanoScope 8.1 software (Veeco) utilizes the DMT model to estimate the Young's moduli. Average estimated Young's moduli were obtained using NanoScope Analysis 1.10 software (Veeco). Three separate films samples were used for all measurements with 3 to 5 images taken per sample.

MC3T3-E1 Cell Culture on $(PrS/SPS)_n$ PEMs

A mouse pre-osteoblast cell line (MC3T3-E1 Subclone 4; American Type Culture Collection; ATCC; CRL-2594) was used for all PEM-cell interaction studies. MC3T3-E1 cells were cultured in TCPS in a growth medium consisting of α-MEM, 10% FBS, and 1% of antibiotic-antimycotic solution and maintained in a humidified incubator (37°C; 5% CO_2 in air). Culture medium was replenished every 2–3 days. MC3T3-E1 cells were sub-cultured when near 100% confluence with the use of 0.05% trypsin-EDTA solution. All MC3T3-E1 cells used in these studies were less than passage number 12.

Cell Adhesion Assays

MC3T3-E1 cells were seeded at a density of 50,000, 200,000, and 500,000 cells/well in 6-well TCPS plates containing 24 mm × 25 mm glass substrates which were either non- coated

controls or coated with 40, 80, or 240 bilayers of $(PrS/SPS)_n$. The test of cell adhesion to the substrates was performed in both α-MEM without FBS and with 10% FBS. Cells were cultured at 37°C and 5% CO_2 in humidified air for two hours prior to determination of cellular metabolic activity by the use of the MTT assay and direct measurement of cell numbers by the Live/Dead® Viability/Cytotoxicity Kit supplemented with Hoechst 33342 as previously described [13].

Cell Proliferation Assays

The ability of MC3T3-E1 cells to proliferate on $(PrS/SPS)_n$ PEMs was evaluated by the MTT assay and Live/Dead® Viability/Cytotoxicity assay described above. MC3T3-E1 cells in growth media were seeded (50,000 cells/well) into 6-well TCPS plates containing PEMs and allowed to proliferate until becoming fully confluent. Samples were sequentially evaluated using the MTT assay and the Live/Dead® assay at time points from 48 hours to more than one-week after being seeded onto the PEMs and control surfaces (uncoated glass and TCPS).

Cell Differentiation Assays

Experiments were also performed in order to evaluate the ability of MC3T3-E1 cells to differentiate into mature osteoblasts while adherent to the surface of (PrS/SPS) PEMs. Cells were initially seeded (500,000 cells/well) onto uncoated and film-coated glass substrates 48 hours prior to the induction of MC3T3-E1 differentiation by replacing the growth media with differentiating media (growth media described above supplemented with 50 μg/ml L-ascorbic acid and 10 mM β-glycerophosphate). The presence of alkaline phosphatase (an early marker of osteogenic differentiation) was evaluated quantitatively (enzyme activity) five days after addition of the differentiation media. The accumulation of calcium within the differentiating MC3T3-E1 cell culture was likewise assessed both qualitatively and quantitatively by Alizarin red S (ARS; Sigma). The maturation of the deposited calcium was demonstrated by the staining of the hydroxyapaptite crystals (containing calcium and phosphorous) by the silver nitrate–based Von Kossa staining protocol.

Statistical Analysis

All data analysis was performed in GraphPad Prism 5 Software (San Diego, CA). Data are reported as mean ± standard deviation of a minimum of at least 3 samples. Statistical significance ($P < 0.05$) was determined by GraphPad Prism 5 software using either Student's two-tailed t-tests or one-way ANOVA using nonparametric Kruskal-Wallis test and Dunns' post-hoc analysis.

3. Results and Discussion

3.1. Film Thickness and Growth Behavior of $(PrS/SPS)_n$ PEMs

Bilayer architecture PEMs were constructed using the cationic PrS and SPS, and the nature of film growth and their surfaces were characterized. Cleaned silicon substrates were functionalized with these $(PrS/SPS)_n$ films over a wide range of bilayer numbers (n). A schematic of the components used in film assembly and the film architecture are shown in Fig. 1. The thickness of the $(PrS/SPS)_n$ PEMs increased linearly as seen in Fig. 2a, with a relatively small incremental increase per bilayer pair (1.91 ± 0.06 nm per bilayer; $R^2 = 0.77$). The accumulation of the individual components within the thin film was monitored by UV-Vis spectroscopy of films deposited on quartz substrates (Fig. 2b). This allowed serial monitoring of the increase in PrS (amide bond and aromatic ring absorption maxima at 200 nm and 280 nm, respectively) and SPS (absorption maximum at 226 nm) [36]. There were progressive increases in absorption intensity at the 200 nm, 226 nm, and 280 nm

wavelengths with increasing bilayer number as shown in Fig. 2b. However, the amide bond wavelength (200 nm; 0.043 ± 0.003 a.u./nm) was an exceedingly more sensitive measure of the accumulation of PrS than the aromatic ring (280 nm; 0.005 ± 0.001 a.u./nm) wavelength because protamine contains primarily aliphatic amino acids and only one aromatic amino acid [37]. The rates of increase in the film components were determined from the slopes of linear regression lines in Fig. 2b and showed that PrS (0.043 ± 0.003 a.u./bilayer) increased at the same order of magnitude as SPS (0.019 ± 0.002 a.u./bilayer), suggestive of similar mass contribution of both components to the increase in thickness of the $(PrS/SPS)_n$ PEMs.

Circular dichroism (CD) analysis was used to determine whether the electrostatic deposition of the PrS polypeptide within the structure of the $(PrS/SPS)_n$ PEMs altered its secondary structure. Deposition of single layers of PrS (Fig. 2c) confirmed previously published results showing that the de novo secondary structure of PrS is that of a random coil [38]. CD spectra of dry $(PrS/SPS)_n$ PEM functionalized quartz surfaces showed that the characteristic random coil spectra of PrS in solution was obtained for PrS in the solid state (Fig. 2c-d). The amplitude of the spectra continually increased with an increasing number of deposited layers within the PEMs. Although an additional optically active species was seen in the $(PrS/SPS)_{80}$ PEM, the spectra still maintained the characteristic random coil secondary structure. This result differs from observations of polypeptide multilayer films fabricated from short peptides, which possessed a random coil conformation in solution and a β sheet conformation in the PEM [39]. Spectroscopic analyses of $(PrS/SPS)_n$ PEMs confirmed that protamine maintained its native secondary structure when complexed with SPS in the dry, solid thin films. The $(PrS/SPS)_n$ film linear growth produced relatively thin coatings over many cycles of polymer deposition, consistent with the complexation of two fully ionized polyelectrolytes with high charge density [40].

Quartz crystal microbalance with dissipation monitoring (QCM-D) was used for real-time monitoring of $(PrS/SPS)_n$ deposition on silicon dioxide coated crystals, the results from which are shown in Supplementary Data (Fig. S1.) [41]. QCM-D was used to fabricate $(PrS/SPS)_{20}$ PEMs with simultaneous monitoring of the frequency (f), which is related to the true mass of polymer deposited on the crystal (m), and the energy dissipation (D) which is related to the viscoelasticity of the deposited mass [42]. SPS was the primary contributor to the progressive increase in dissipation ($\Delta D = 2.21 \pm 0.33 \times 10^{-6}$ per SPS layer) during PEM growth; whereas, the adsorption of PrS resulted in a consistent reduction in the dissipation ($\Delta D = -0.26 \pm 0.06 \times 10^{-6}$ per PrS layer) during PEM growth (Fig. S1c). Hence, the PEM became somewhat more rigid when PrS was the outer layer, but softer and more dissipative when SPS was the outer layer. The Sauerbrey relation can be assumed to be a good approximation for the $(PrS/SPS)_n$ PEMs due to the relatively small changes in ΔD [43]. The post-rinse frequency decreased linearly at a rate of 29.6 ± 0.4 Hz/bilayer ($R^2 = 0.99$), analogous to an estimated mass deposited of 74.8 ± 1.1 ng/cm^2-bilayer computed from Sauerbrey's relation ($R^2 = 0.99$). Both polymer deposition cycles resulted in near equal change in the frequency ($\Delta f = -12.3 \pm 4.0$ and -16.4 ± 0.9 Hz for SPS and PrS, respectively), suggesting that each polymer contributes similar polymer mass to the linearly growing $(PrS/SPS)_n$ PEMs (31.1 ± 10.1 and 41.6 ± 2.4 ng/cm^2 for each adsorbed layer of SPS and PrS, respectively. These QCM-D results are consistent with the linear increases in PrS and SPS absorbance monitored via UV-Vis and clearly suggest that PrS and SPS, while contributing a similar mass during film growth, result in markedly different alterations in the viscoelastic properties of the thin film with each deposition step.

3.2. Thin Film Surface Characterization of $(PrS/SPS)_n$ PEMs

The films produced are relatively smooth at lower *n*, but become much rougher at higher *n* as shown in Fig. 3. A uniform surface morphology consisting of minute surface elevations with maximum heights (z_{max}) in the range of 30 to 110 nm are seen for all $(PrS/SPS)_n$ with

$n \leq 100$ bilayers. A much broader distribution of islands and larger surface features with z_{max} between 1000 to 1600 nm were seen for $n \leq 100$ bilayers. AFM images of scratched $(PrS/SPS)_n$ PEMs fabricated on silicon substrates demonstrated complete surface coverage in all cases (Fig. 4 a – b); thus, although the thicker films are rough, they do not show signs of degradation or deconstruction during the assembly process. Surface roughness measurements of the dry $(PrS/SPS)_n$ films were obtained by AFM and are shown in Fig. 4 (c – d, where d contains a close-up of the film roughness in the first 100 layers). The RMS roughness (R_q) progressively decreased as the thickness increased from 20 to 60 bilayers (13.4 ± 1.1 nm to 4.6 ± 1.1 nm), remained relatively constant at intermediate film thicknesses (4.6 ± 1.1 nm, 4.8 ± 0.4 nm, and 5.7 ± 0.8 nm at 60, 80, and 100 bilayers, respectively), and drastically increased at the higher bilayer numbers (194.0 ± 6.5 nm, 220.0 ± 2.8 nm, and 138.5 ± 21.9 nm at 180, 200, and 240 bilayers, respectively). This irregular pattern of change in the roughness of $(PrS/SPS)_n$ PEMs is markedly different from the constant roughness or linear increase in roughness with increase in thickness typically reported for PEMs [9]. In order to determine whether PrS interlayer diffusion or exchange plays a role in the change of roughness of the films with number of layers, we examined the RMS roughness of 200 and 240 bilayer $(PrS/SPS)_n$ PEMs, and the same PEMs after equilibrating in a 10 mM PrS solution and phosphate buffered saline (PBS) for approximately 24 hours. (Supplementary Data, Fig. S2). PrS equilibrated PEMs demonstrated significant increases in surface roughness compared to the native PEMs; similar results were also observed when films were conditioned in the presence of PBS. The fact that these films become rougher when they are simply “annealed” in protamine or buffered salt solutions suggests that over extended periods, the PrS may be sufficiently mobile within the multilayer to allow significant rearrangements of the film during its construction at thicker layers. There may be a critical film thickness beyond which this film rearrangement is favored based on the balance between surface interactions and the interactions of the film components within the film matrix. A mechanism involving significant amounts of interdiffusion of PrS within the PEM would typically suggest an exponential increase in thickness with increasing bilayer number [44]; however, this behavior was not observed here.

Dynamic (advancing and receding) air-water contact angle measurements were performed in order to assess the wettability of $(PrS/SPS)_n$ PEMs as shown in Figure 5a [45]. The advancing contact angles of 10 to 80 bilayer films (30–50°) were significantly higher than the associated receding contact angles (5–10°). Dynamic air-water contact angles were not measurable for 100 to 240 bilayer PEMs due to the extreme hydrophilicity of these surface coatings. Hence, the contact angle of $(PrS/SPS)_n$ films progressively decreased with increasing number of bilayers, rendering them extremely hydrophilic. In situ liquid-phase spectroscopic ellipsometry was used to investigate the post-fabrication swelling that takes place upon hydration of a dry film [46, 47]. Thicknesses of PEMs submerged in PBS were determined after 5 minutes of hydration (Fig. 5b). The dry-state thicknesses of the PEMs as measured by ellipsometry prior to hydration were consistent with the thicknesses measured by profilometry, and demonstrated the same linear increase with increasing number of bilayers (1.3 ± 0.04 nm/bilayer, $R^2 = 0.98$). Hydrated thickness of these PEMs showed linear thickness increase with increasing bilayer number, as well (2.1 ± 0.2 nm/bilayer, $R^2 = 0.91$). The hydrated PEMs were approximately 60.7 ± 18.3% thicker than the corresponding dry films. The thicker (≥ 300 nm) PEMs were generally swollen to a greater extent (60 – 80%) compared to the thinner (≤ 200 nm) PEMs (40 – 50%). The mechanical properties of the swollen $(PrS/SPS)_n$ PEMs were evaluated via liquid-phase AFM. The estimated Young’s moduli of the PEMs increased exponentially ($R^2 = 0.98$) from 20 to 80 bilayers shown in Fig. 5c. In particular, the Young’s modulus increased significantly from 1.8 ± 0.3 MPa at 20 bilayers to 43.3 ± 6.9 MPa at 80 bilayers. For comparison, the estimated Young’s modulus for the dry 80 bilayer film was 4,850 ± 90 MPa; hence, the hydration of the film results in

about a 100-fold decrease in the stiffness of the thin film due to the uptake of water in the LbL ionically crosslinked matrix. The estimated Young's modulus of these hydrated (PrS/SPS)$_n$ PEMs was significantly higher than the 3–400 kPa reported for chemically cross-linked poly(L-lysine)/hyaluronan films, but similar to the 6–100 MPa range reported for hydrated, synthetic weak polyelectrolyte PEMs studied by VanVliet and Rubner [48]. Hydrated (PrS/SPS)$_n$ PEM stiffness increased exponentially with bilayer number to magnitudes that usually require post-fabrication cross-linking of the PEM through chemical exposure or heat treatment [20]. The increased surface roughness and stiffness with growth of the (PrS/SPS)$_n$ PEMs are expected to be compatible with enhancing cell-PEM interactions. The moderately hydrophilic nature of the (PrS/SPS)$_n$ PEMs should also prove useful in promoting cell-PEM interactions.

A rigid support is essential for the proper interaction of cells with their underlying scaffold [49]. Our QCM-D analysis showed that incorporation of SPS accounted for the majority of the reduction in the stiffness during assembly, while the addition of PrS markedly increased the PEM stiffness. Conformational changes in the adsorbed polymer layers, as evidenced by changes in dissipation, suggest that SPS may adsorb in a partially shielded, loopy conformation on the surface while the adsorbed PrS appears to be more closely bound to the (PrS/SPS)$_n$ PEM surface, potentially forming compact ionic complexes with SPS [50]. The stiffening of the PEM upon the incorporation of PrS is consistent with PrS behaving as a short, stiff rod-like polyelectrolyte due to the high level of intra-polymer repulsion and the helical backbone in the presence of fully ionized arginine side groups in the acidic (pH 5.0) LbL assembly environment. Hence, the QCM-D results strongly suggest that the unique mechanical properties of the native, non-cross-linked (PrS/SPS)$_n$ PEMs, as evidenced by the exponential increase in the Young's modulus in our AFM studies, may arise from the intrinsic rigidity of the short polypeptide PrS as governed by electrostatic repulsive forces.

3.3. Osteoconductive properties of (PrS/SPS)$_n$ PEMs

3.3.1. Pre-osteoblast adhesion—(PrS/SPS)$_n$ PEMs were investigated for their ability to support the adhesion of cells in culture as a function of number of bilayers or film thickness. MC3T3-E1 cells maintained their normal polygonal morphology with multiple cellular projections both on control substrates (tissue culture polystyrene (TCPS) and uncoated glass) and on (PrS/SPS)$_n$ functionalized surfaces (Fig. 6). Sub-confluent monolayers of MC3T3-E1 pre-osteobalst cells assumed an elongated, spindle-like morphology with low cytoplasm area when adherent to TCPS and uncoated glass substrates. In contrast, these cells assumed a cuboidal morphology with marked increase in cytoplasm area and numerous surface projections when adherent to PrS/SPS coated substrates. The lower (20 and 40) bilayer PrS/SPS coated surfaces show MC3T3-E1 cells with numerous cytoplasm projections asymmetrically distributed around the cell nucleus. The higher (80 and 240) bilayer PrS/SPS coated surfaces showed a decreased number and shorter cytoplasm projections, but the cells maintained a high cytoplasm area.

The adhesion of MC3T3-E1 cells to each substrate (either uncoated glass or PEM coated glass) was quantified by cellular metabolic activity (MTT assay) normalized to total culture area as shown in Fig. 7a-b. Serum-free cultures of MC3T3-E1 cells on (PrS/SPS)$_n$ PEM functionalized surfaces demonstrated an identical level of cell adhesion as serum-free cultures on uncoated glass surfaces at the lowest cell seeding density (5,000 cells/cm^2). In marked contrast, (PrS/SPS)$_n$ PEM functionalized surfaces possessed significantly higher serum-free cell adhesion than uncoated glass at the higher cell seeding densities (20,000 and 50,000 cells/cm^2). There was generally no statistical difference between MC3T3-E1 adhesion in serum-containing medium on uncoated glass and (PrS/SPS)$_n$ PEM functionalized surfaces, except at the highest seeding density (Fig. 7 b). Cells generally

adhere poorly to non-cross-linked PEMs in direct correlation to their native mechanical properties [20]. The three-fold increase in the stiffness of $(PrS/SPS)_n$ PEMs compared to conventional PEMs appears to be primarily responsible for the normalization of cell adhesion to that of cultures on uncoated glass and/or TCPS. Others have previously reported enhanced MC3T3-E1 adhesion to amine terminated silicon oxide substrates with nanometer-scale surface roughness [51]. Enhanced osteoblast adhesion and focal adhesion formation have been demonstrated on nanometer-scale structures on implant surfaces [52, 53]. There was generally no statistical difference in cell adhesion between 40, 80, and 240 bilayer PEMs at all seeding densities, indicating negligible effect of large changes in nanometer-scale roughness on MC3T3-E1 adhesion.

Cell adhesion to all surfaces was best at the highest (50,000 cells/cm^2) compared to the lower (5,000 and 20,000 cells/cm^2) seeding densities. PEMs generally supported low levels of cell adhesion at low cell seeding density where cell-matrix interactions (integrin binding and focal adhesion formation) are expected to be the major contributor to cell adhesion, but higher levels of cell adhesion at the high seeding density where cell-cell interactions (cadherins) are expected to be a substantial contributor to cell adhesion [54]. Cell adhesion to all surfaces was much higher in 10% fetal bovine serum cultures than in serum-free cultures as shown in Fig. 7b. Hence, binding of serum proteins to the surfaces greatly facilitated initial cell-surface interaction [55]. It appears that the nature of the proteins and/or the magnitude of the protein binding to the hydrophilic uncoated glass and PEMs differs markedly from that of the hydrophobic TCPS surface [55].

3.3.2. Pre-osteoblast proliferation—MC3T3-E1 pre-osteoblast cells display two distinct growth phases during in vitro osteogenic differentiation [56]. After MC3T3-E1 cells become attached to an osteoconductive surface, they enter a rapid proliferative growth phase in order to establish critical cell-cell interactions essential for the subsequent post-confluent differentiation growth phase. Encouraged by the ability of native $(PrS/SPS)_n$ PEM functionalized surfaces to adequately support the adhesion of MC3T3-E1 cells, PEMs were assessed for their ability to support proliferation of cells seeded at a low density (5,000 cells/cm^2). MC3T3-E1 cell proliferation was monitored directly via fluorescence microscopy imaging of individual cells directly attached to the culture surfaces and indirectly via the use of the MTT assay to measure the metabolic activity of the total population of cells growing on the surfaces (Fig. 7c-d, respectively). MC3T3-E1 cells proliferated most rapidly on TCPS (13.7 ± 0.6 cells/$140\mu m^2$/hr, $R^2 = 0.95$). In contrast, MC3T3-E1 cells proliferated at similar rates on uncoated glass and 40-bilayer functionalized surfaces (7.0 ± 0.4 and 6.1 ± 0.3 cells/$140\mu m^2$/hr, respectively; $R^2 = 0.89$ and 0.84, respectively), but at the slowest rate on 80-bilayer films (3.2 ± 0.2 cells/$140\mu m^2$/hr, $R^2 = 0.68$). The inverse relation between nanometer-scale surface roughness and osteoblast proliferation demonstrated here have been previously noted on surfaces with micron-scale and nanometer-scale surface roughness [57]. Lower osteoblast proliferation is generally seen on rough surfaces than on smooth surfaces [58]. The MTT activity was higher at 3 weeks than at 1 week in culture (Fig. 7d), indicating the MC3T3-E1 pre-osteoblasts were able to sustain growth on $(PrS/SPS)_n$ PEMs over a wide range of PEM thicknesses (n = 20, 40, 80, 160, and 240).

3.3.3. Pre-osteoblast differentiation—$(PrS/SPS)_n$ PEMs were investigated for their ability to support the differentiation of cells in culture. After initial high seeding density (50,000 cells/cm^2) in serum-containing growth media and a 48-hour culture stabilization period, the cells were cultured for a subsequent 4 weeks in osteogenic differentiation media. Osteogenic differentiation of MC3T3-E1 cells was assessed by alkaline phosphatase (ALP) enzyme activity, Alizarin Red S (ARS) staining and quantification, and von Kossa staining. Increased ALP enzyme activity is an early marker of osteogenic differentiation. Anionic ARS efficiently stains the calcium deposits in the newly deposited extracellular matrix

(ECM) of differentiated osteoblasts. Mineralization of calcified ECM, due to the incorporation of phosphate ions to form the hydroxapatite bone mineral, is commonly visualized by von Kossa staining [59]. Three critical processes are required for bone formation: the presence of osteogenic stem and/or progenitor cells, ostoinductive growth factors to stimulate the differentiation of these cells along an osteoblastic pathway, and an osteoconductive surface to support cell growth and the deposition of new bone matrix. Five days after the induction of osteogenic differentiation, ALP activity of cells on all $(PrS/SPS)_n$ PEMs was significantly lower than cells on the uncoated glass as seen in Fig. 8a. A reduction in ALP enzyme activity was previously reported for osteoblasts cultured for 7 days on hydrophilic substrates with micrometer-scale surface roughness [57]. In contrast, quantification of the ARS staining showed that the amount of ARS (calcium deposits) on all $(PrS/SPS)_n$ PEMs were significantly greater than that on control uncoated glass slides at 15, 22, and 27 days after the induction of osteogenic differentiation (Fig. 8b-d). There was no statistical difference among the $(PrS/SPS)_n$ PEM ARS staining at 15 days as seen in Fig. 8b. The ARS staining on all $(PrS/SPS)_n$ PEM functionalized surfaces were greatest at 22 days (Fig. 8c) and was 5 to 10 times higher than ARS levels on uncoated glass surfaces. The ARS staining on the 80 bilayer functionalized glass surfaces were significantly lower than that of the 40 and 240 bilayer PEMs, in a pattern that parallels the surface roughness of these PEMs. A direct association between increased micro-scale roughness and increased osteoblast differentiation has been previously demonstrated by others [60].

Focal ARS staining of the extracellular matrix was noted in the MC3T3-E1 monolayers on $(PrS/SPS)_n$ PEM functionalized surfaces shown in Fig. 9. The intensity of the ARS staining and the size of the focal deposits increased with increasing film thickness. The von Kossa staining was also enhanced on the $(PrS/SPS)_n$ PEM functionalized surfaces, but not with as wide differences in staining intensity with increasing bilayers as seen with the ARS staining. Nevertheless, the focal areas of von Kossa staining closely match those depicted in the ARS images. Osteointegration of a metallic implant with host bone depends both on the recruitment of stem cells and the induction of these cells to differentiate into osteoblasts (osteoinduction) and on the ability of the implant surface to support the adhesion, proliferation, and differentiation of the osteoblasts leading to the deposition of a mineralized bone matrix on the implant surface (osteoconduction) [61]. The enhanced ARS and von Kossa staining of long-term MC3T3-E1 cultures strongly suggest that $(PrS/SPS)_n$ functionalized surfaces possess particular physiochemical characteristics that favor the differentiation of osteoblastic progenitors and/or favor the mineralization of the ECM deposited by mature osteoblasts, thus possessing intrinsic osteoconductive properties. The magnitude of calcium deposition increases in direct relation to the amount of PrS and SPS within the functionalized PEM surface. The anionic SPS within the PEMs could potentially serve as binding sites to sequester free calcium and would likely result in diffuse homogeneous calcium deposition, not the large focal calcium deposits observed. Alternatively, the highly positively charged PrS may serve as a binding site for acidic phospholipids and matrix vesicles, both critical for the nucleation of mineralization [59]. The focal nature of the calcium deposits observed on the $(PrS/SPS)_n$ PEM functionalized surfaces is more consistent with a PrS-matrix vesicle sequestration process. These matrix vesicles, produced from the cell membrane of the MC3T3-E1 cells, are enriched with acidic phospholipids and contain a high concentration of calcium needed for the nucleation of bone mineral in the extracellular matrix.

Increased ARS staining of the cell layer directly correlated with increasing surface roughness and hydrophilicity of $(PrS/SPS)_n$ PEMs. The combination of high nanometer-scale roughness and hydrophilicity resulted in the greatest enhancement of osteoblast differentiation. Moreover, the magnitude of osteogenic differentiation on hydrophilic surfaces can be modulated by relatively small changes in the nanometer-scale roughness.

Material surface chemistry and topography are key regulators of osteoblast differentiation at the cell-implant interface [62]. In particular, the osteoconductivity of hydrophilic high surface energy surfaces have been demonstrated by enhanced osteoblastic differentiation in vitro and by improved osteointegration of titanium implants in animal models, as evidenced by increased removal torque forces and bone-to-implant contact values [58, 63]. Recent reports have demonstrated the modulation of human mesenchymal stem cell (hMSC) fate on nanometer-scale structures, wherein 10 nm structures stimulated osteoblastic differentiation, 30 nm nanotubes promoted enhanced adhesion without associated differentiation, and 70 – 100 nm nanotubes induced hMSC elongation [64, 65]. It is possible that $(PrS/SPS)_n$ PEM functionalized surfaces with their hydrophilic surface chemistry and nanometer-scale surface roughness may likewise modulate stem cell fate.

4. Conclusions

The protamine-based PEM thin film coatings developed in this work demonstrate excellent osteoconductivity, i.e., the ability to act as a scaffold to support the robust adhesion, proliferation, and differentiation of MC3T3-E1 pre-osteoblast cells. This protamine-based PEM system that does not require harsh post-fabrication cross-linking treatments to increase PEM stiffness; these films paradoxically increase in stiffness with increased thickness of the PEM, thus greatly facilitating MC3T3-E1 cell-substrate interactions. The nanoscale surface roughness and hydrophilic nature of these protamine-based PEMs greatly facilitates osteoblast deposition of a mineralized bone matrix. These PEMs represent an alternate biomaterials approach for surface functionalization of implants aimed at improving osteointegration in bone tissue engineering and total joint arthroplasty applications. Protamine-based PEM functionalized surfaces can make an immediate impact in the fields of in vitro osteogenic culture of stem cells and assessing the osteogenic potential of bioactive agents.

Supplementary Material

Refer to Web version on PubMed Central for supplementary material.

Acknowledgments

This work was supported by grants (5R01AG029601) to P.T. Hammond from US National Institutes of Health National Institute of Aging (NIH NIA). R.E. Samuel thanks the NIH NIA for support via a Research Supplement to Promote Diversity in Health-Related Research. A. Shukla gratefully acknowledges support from a National Science Foundation Graduate Research Fellowship. Use of the Center for Materials Science and Engineering Shared Experimental Facilities and Institute for Soldier Nanotechnologies at MIT are greatly appreciated.

References

1. Petrie TA, Raynor JE, Reyes CD, Burns KL, Collard DM, Garcia AJ. The effect of integrin-specific bioactive coatings on tissue healing and implant osseointegration. Biomaterials. 2008; 29(19):2849–57. [PubMed: 18406458]
2. Roach P, Eglin D, Rohde K, Perry CC. Modern biomaterials: a review - bulk properties and implications of surface modifications. J Mater Sci Mater Med. 2007; 18(7):1263–77. [PubMed: 17443395]
3. de Jonge LT, Leeuwenburgh SC, van den Beucken JJ, te Riet J, Daamen WF, Wolke JG, et al. The osteogenic effect of electrosprayed nanoscale collagen/calcium phosphate coatings on titanium. Biomaterials. 2010; 31(9):2461–9. [PubMed: 20022365]
4. Ramaswamy Y, Wu C, Dunstan CR, Hewson B, Eindorf T, Anderson GI, et al. Sphene ceramics for orthopedic coating applications: an in vitro and in vivo study. Acta Biomater. 2009; 5(8):3192–204. [PubMed: 19457458]

5. Lavos-Valereto IC, Wolynec S, Deboni MC, Konig B Jr. In vitro and in vivo biocompatibility testing of Ti-6Al-7Nb alloy with and without plasma-sprayed hydroxyapatite coating. J Biomed Mater Res. 2001; 58(6):727–33. [PubMed: 11745527]
6. Brama M, Rhodes N, Hunt J, Ricci A, Teghil R, Migliaccio S, et al. Effect of titanium carbide coating on the osseointegration response in vitro and in vivo. Biomaterials. 2007; 28(4):595–608. [PubMed: 17049981]
7. Macdonald ML, Samuel RE, Shah NJ, Padera RF, Beben YM, Hammond PT. Tissue integration of growth factor-eluting layer-by-layer polyelectrolyte multilayer coated implants. Biomaterials. 2010; 32(5):1446–53. [PubMed: 21084117]
8. Leguen E, Chassepot A, Decher G, Schaaf P, Voegel JC, Jessel N. Bioactive coatings based on polyelectrolyte multilayer architectures functionalized by embedded proteins, peptides or drugs. Biomol Eng. 2007; 24(1):33–41. [PubMed: 16860599]
9. Cini N, Tulun T, Decher G, Ball V. Step-by-step assembly of self-patterning polyelectrolyte films violating (almost) all rules of layer-by-layer deposition. J Am Chem Soc. 2010; 132(24):8264–5. [PubMed: 20518535]
10. Ariga K, Hill JP, Ji Q. Layer-by-layer assembly as a versatile bottom-up nanofabrication technique for exploratory research and realistic application. Phys Chem Chem Phys. 2007; 9(19):2319–40. [PubMed: 17492095]
11. Schlenoff JB. Retrospective on the future of polyelectrolyte multilayers. Langmuir. 2009; 25(24): 14007–10. [PubMed: 19670891]
12. Ai H, Jones SA, Lvov YM. Biomedical applications of electrostatic layer-by-layer nano-assembly of polymers, enzymes, and nanoparticles. Cell Biochem Biophys. 2003; 39(1):23–43. [PubMed: 12835527]
13. Moskowitz JS, Blaisse MR, Samuel RE, Hsu HP, Harris MB, Martin SD, et al. The effectiveness of the controlled release of gentamicin from polyelectrolyte multilayers in the treatment of Staphylococcus aureus infection in a rabbit bone model. Biomaterials. 2010; 31(23):6019–30. [PubMed: 20488534]
14. Macdonald M, Rodriguez NM, Smith R, Hammond PT. Release of a model protein from biodegradable self assembled films for surface delivery applications. J Control Release. 2008; 131(3):228–34. [PubMed: 18721835]
15. Mehrotra S, Lynam D, Maloney R, Pawelec KM, Tuszynski MH, Lee I, et al. Time controlled protein release from layer-by-layer assembled multilayer functionalized agarose hydrogels. Adv Funct Mater. 2010; 20(2):247–58. [PubMed: 20200599]
16. Wood KC, Boedicker JQ, Lynn DM, Hammond PT. Tunable drug release from hydrolytically degradable layer-by-layer thin films. Langmuir. 2005; 21(4):1603–9. [PubMed: 15697314]
17. Mansouri S, Winnik FM, Tabrizian M. Modulating the release kinetics through the control of the permeability of the layer-by-layer assembly: a review. Expert Opin Drug Deliv. 2009; 6(6):585–97. [PubMed: 19480609]
18. Blacklock J, Sievers TK, Handa H, You YZ, Oupicky D, Mao G, et al. Cross-linked bioreducible layer-by-layer films for increased cell adhesion and transgene expression. J Phys Chem B. 2010; (16):5283–91. [PubMed: 20369813]
19. Alves NM, Picart C, Mano JF. Self assembling and crosslinking of polyelectrolyte multilayer films of chitosan and alginate studied by QCM and IR spectroscopy. Macromol Biosci. 2009; 9(8):776–85. [PubMed: 19340816]
20. Boudou T, Crouzier T, Auzely-Velty R, Glinel K, Picart C. Internal composition versus the mechanical properties of polyelectrolyte multilayer films: the influence of chemical cross-linking. Langmuir. 2009; 25(24):13809–19. [PubMed: 20560550]
21. Hillberg AL, Holmes CA, Tabrizian M. Effect of genipin cross-linking on the cellular adhesion properties of layer-by-layer assembled polyelectrolyte films. Biomaterials. 2009; 30(27):4463–70. [PubMed: 19520425]
22. Zheng H, Berg MC, Rubner MF, Hammond PT. Controlling cell attachment selectively onto biological polymer-colloid templates using polymer-on-polymer stamping. Langmuir. 2004; 20(17):7215–22. [PubMed: 15301508]

23. Berg MC, Yang SY, Hammond PT, Rubner MF. Controlling mammalian cell interactions on patterned polyelectrolyte multilayer surfaces. Langmuir. 2004; 20(4):1362–8. [PubMed: 15803720]
24. Mendelsohn JD, Yang SY, Hiller J, Hochbaum AI, Rubner MF. Rational design of cytophilic and cytophobic polyelectrolyte multilayer thin films. Biomacromolecules. 2003; 4(1):96–106. [PubMed: 12523853]
25. Gemici Z, Shimomura H, Cohen RE, Rubner MF. Hydrothermal treatment of nanoparticle thin films for enhanced mechanical durability. Langmuir. 2008; 24(5):2168–77. [PubMed: 18232719]
26. Vazquez CP, Boudou T, Dulong V, Nicolas C, Picart C, Glinel K. Variation of polyelectrolyte film stiffness by photo-cross-linking: a new way to control cell adhesion. Langmuir. 2009; 25(6):3556–63. [PubMed: 19275180]
27. Thompson MT, Berg MC, Tobias IS, Lichter JA, Rubner MF, Van Vliet KJ. Biochemical functionalization of polymeric cell substrata can alter mechanical compliance. Biomacromolecules. 2006; 7(6):1990–5. [PubMed: 16768424]
28. Carrell DT, Emery BR, Hammoud S. The aetiology of sperm protamine abnormalities and their potential impact on the sperm epigenome. Int J Androl. 2008; 31(6):537–45. [PubMed: 18298569]
29. Brange J, Langkjaer L. Insulin formulation and delivery. Pharm Biotechnol. 1997; 10:343–409. [PubMed: 9160379]
30. Davis D, Akhtar U, Keaster B, Grozinger K, Washington L, Kelsey S, et al. Challenges and potential for RNA nanoparticles (RNPs). J Biomed Nanotechnol. 2009; 5(1):36–44. [PubMed: 20055104]
31. Moran MC, Pais AA, Ramalho A, Miguel MG, Lindman B. Mixed protein carriers for modulating DNA release. Langmuir. 2009; 25(17):10263–70. [PubMed: 19627156]
32. Balabushevich NG, Larionova NI. Protein-loaded microspheres prepared by sequential adsorption of dextran sulphate and protamine on melamine formaldehyde core. J Microencapsul. 2009; 26(7): 571–9. [PubMed: 19839792]
33. Shutava TG, Balkundi SS, Vangala P, Steffan JJ, Bigelow RL, Cardelli JA, et al. Layer-by-layer-coated gelatin nanoparticles as a vehicle for delivery of natural polyphenols. ACS Nano. 2009; 3(7):1877–85. [PubMed: 19534472]
34. Shukla A, Fleming KE, Chuang HF, Chau TM, Loose CR, Stephanopoulos GN, et al. Controlling the release of peptide antimicrobial agents from surfaces. Biomaterials. 2010; 31(8):2348–57. [PubMed: 20004967]
35. DeMuth PC, Su X, Samuel RE, Hammond PT, Irvine DJ. Nano-layered microneedles for transcutaneous delivery of polymer nanoparticles and plasmid DNA. Adv Mater. 2010; 22(43): 4851–6. [PubMed: 20859938]
36. Niemiec W, Zapotoczny S, Szczubialka K, Laschewsky A, Nowakowska M. Nanoheterogeneous multilayer films with perfluorinated domains fabricated using the layer-by-layer method. Langmuir. 2010; 26(14):11915–20. [PubMed: 20527832]
37. Brewer L, Corzett M, Balhorn R. Condensation of DNA by spermatid basic nuclear proteins. J Biol Chem. 2002; 277(41):38895–900. [PubMed: 12140285]
38. Toniolo C, Bonora GM, Marchiori F, Borin G, Filippi B. Protamines. II. Circular dichroism study of the three main components of clupeine. Biochim Biophys Acta. 1979; 576(2):429–39. [PubMed: 427200]
39. Haynie DT, Zhang L, Zhao W, Rudra JS. Protein-inspired multilayer nanofilms: science, technology and medicine. Nanomedicine. 2006; 2(3):150–7. [PubMed: 17292137]
40. Porcel C, Lavalle P, Ball V, Decher G, Senger B, Voegel JC, et al. From exponential to linear growth in polyelectrolyte multilayers. Langmuir. 2006; 22(9):4376–83. [PubMed: 16618190]
41. Dixon MC. Quartz crystal microbalance with dissipation monitoring: enabling real-time characterization of biological materials and their interactions. J Biomol Tech. 2008; 19(3):151–8. [PubMed: 19137101]
42. Johannsmann D, Reviakine I, Rojas E, Gallego M. Effect of sample heterogeneity on the interpretation of QCM(-D) data: comparison of combined quartz crystal microbalance/atomic force microscopy measurements with finite element method modeling. Anal Chem. 2008; 80(23): 8891–9. [PubMed: 18954085]

43. Feiler AA, Sahlholm A, Sandberg T, Caldwell KD. Adsorption and viscoelastic properties of fractionated mucin (BSM) and bovine serum albumin (BSA) studied with quartz crystal microbalance (QCM-D). J Colloid Interface Sci. 2007; 315(2):475–81. [PubMed: 17706239]
44. Porcel C, Lavalle P, Decher G, Senger B, Voegel JC, Schaaf P. Influence of the polyelectrolyte molecular weight on exponentially growing multilayer films in the linear regime. Langmuir. 2007; 23(4):1898–904. [PubMed: 17279672]
45. Seo J, Lutkenhaus JL, Kim J, Hammond PT, Char K. Effect of the layer-by-layer (LbL) deposition method on the surface morphology and wetting behavior of hydrophobically modified PEO and PAA LbL films. Langmuir. 2008; 24(15):7995–8000. [PubMed: 18558781]
46. Schmidt DJ, Cebeci FC, Kalcioglu ZI, Wyman SG, Ortiz C, Van Vliet KJ, et al. Electrochemically controlled swelling and mechanical properties of a polymer nanocomposite. ACS Nano. 2009; 3(8):2207–16. [PubMed: 19624148]
47. Crouzier T, Picart C. Ion pairing and hydration in polyelectrolyte multilayer films containing polysaccharides. Biomacromolecules. 2009; 10(2):433–42. [PubMed: 19199579]
48. Thompson MT, Berg MC, Tobias IS, Rubner MF, Van Vliet KJ. Tuning compliance of nanoscale polyelectrolyte multilayers to modulate cell adhesion. Biomaterials. 2005; 26(34):6836–45. [PubMed: 15972236]
49. Richert L, Lavalle P, Vautier D, Senger B, Stoltz JF, Schaaf P, et al. Cell interactions with polyelectrolyte multilayer films. Biomacromolecules. 2002; 3(6):1170–8. [PubMed: 12425653]
50. Roach P, Farrar D, Perry CC. Interpretation of protein adsorption: surface-induced conformational changes. J Am Chem Soc. 2005; 127(22):8168–73. [PubMed: 15926845]
51. El-Ghannam AR, Ducheyne P, Risbud M, Adams CS, Shapiro IM, Castner D, et al. Model surfaces engineered with nanoscale roughness and RGD tripeptides promote osteoblast activity. J Biomed Mater Res A. 2004; 68(4):615–27. [PubMed: 14986317]
52. Pareta RA, Reising AB, Miller T, Storey D, Webster TJ. An understanding of enhanced osteoblast adhesion on various nanostructured polymeric and metallic materials prepared by ionic plasma deposition. J Biomed Mater Res A. 2010; 92(3):1190–201. [PubMed: 19322818]
53. Biggs MJ, Richards RG, Gadegaard N, Wilkinson CD, Oreffo RO, Dalby MJ. The use of nanoscale topography to modulate the dynamics of adhesion formation in primary osteoblasts and ERK/MAPK signalling in STRO-1+ enriched skeletal stem cells. Biomaterials. 2009; 30(28): 5094–103. [PubMed: 19539986]
54. Saha K, Pollock JF, Schaffer DV, Healy KE. Designing synthetic materials to control stem cell phenotype. Curr Opin Chem Biol. 2007; 11(4):381–7. [PubMed: 17669680]
55. Absolom DR, Zingg W, Neumann AW. Protein adsorption to polymer particles: role of surface properties. J Biomed Mater Res. 1987; 21(2):161–71. [PubMed: 3818679]
56. Quarles LD, Yohay DA, Lever LW, Caton R, Wenstrup RJ. Distinct proliferative and differentiated stages of murine MC3T3-E1 cells in culture: an in vitro model of osteoblast development. J Bone Miner Res. 1992; 7(6):683–92. [PubMed: 1414487]
57. Keselowsky BG, Wang L, Schwartz Z, Garcia AJ, Boyan BD. Integrin alpha(5) controls osteoblastic proliferation and differentiation responses to titanium substrates presenting different roughness characteristics in a roughness independent manner. J Biomed Mater Res A. 2007; 80(3): 700–10. [PubMed: 17133443]
58. Rausch-fan X, Qu Z, Wieland M, Matejka M, Schedle A. Differentiation and cytokine synthesis of human alveolar osteoblasts compared to osteoblast-like cells (MG63) in response to titanium surfaces. Dent Mater. 2008; 24(1):102–10. [PubMed: 17467048]
59. Bonewald LF, Harris SE, Rosser J, Dallas MR, Dallas SL, Camacho NP, et al. von Kossa staining alone is not sufficient to confirm that mineralization in vitro represents bone formation. Calcif Tissue Int. 2003; 72(5):537–47. [PubMed: 12724828]
60. Schwarz F, Wieland M, Schwartz Z, Zhao G, Rupp F, Geis-Gerstorfer J, et al. Potential of chemically modified hydrophilic surface characteristics to support tissue integration of titanium dental implants. J Biomed Mater Res B Appl Biomater. 2009; 88(2):544–57. [PubMed: 18837448]
61. Albrektsson T, Johansson C. Osteoinduction, osteoconduction and osseointegration. Eur Spine J. 2001; 10 (Suppl 2):S96–101. [PubMed: 11716023]

62. Liao H, Andersson AS, Sutherland D, Petronis S, Kasemo B, Thomsen P. Response of rat osteoblast-like cells to microstructured model surfaces in vitro. Biomaterials. 2003; 24(4):649–54. [PubMed: 12437959]

63. Park JW, Jang JH, Lee CS, Hanawa T. Osteoconductivity of hydrophilic microstructured titanium implants with phosphate ion chemistry. Acta Biomater. 2009; 5(6):2311–21. [PubMed: 19332400]

64. Dalby MJ, Gadegaard N, Tare R, Andar A, Riehle MO, Herzyk P, et al. The control of human mesenchymal cell differentiation using nanoscale symmetry and disorder. Nat Mater. 2007; 6(12): 997–1003. [PubMed: 17891143]

65. Oh S, Brammer KS, Li YS, Teng D, Engler AJ, Chien S, et al. Stem cell fate dictated solely by altered nanotube dimension. Proc Natl Acad Sci USA. 2009; 106(7):2130–5. [PubMed: 19179282]

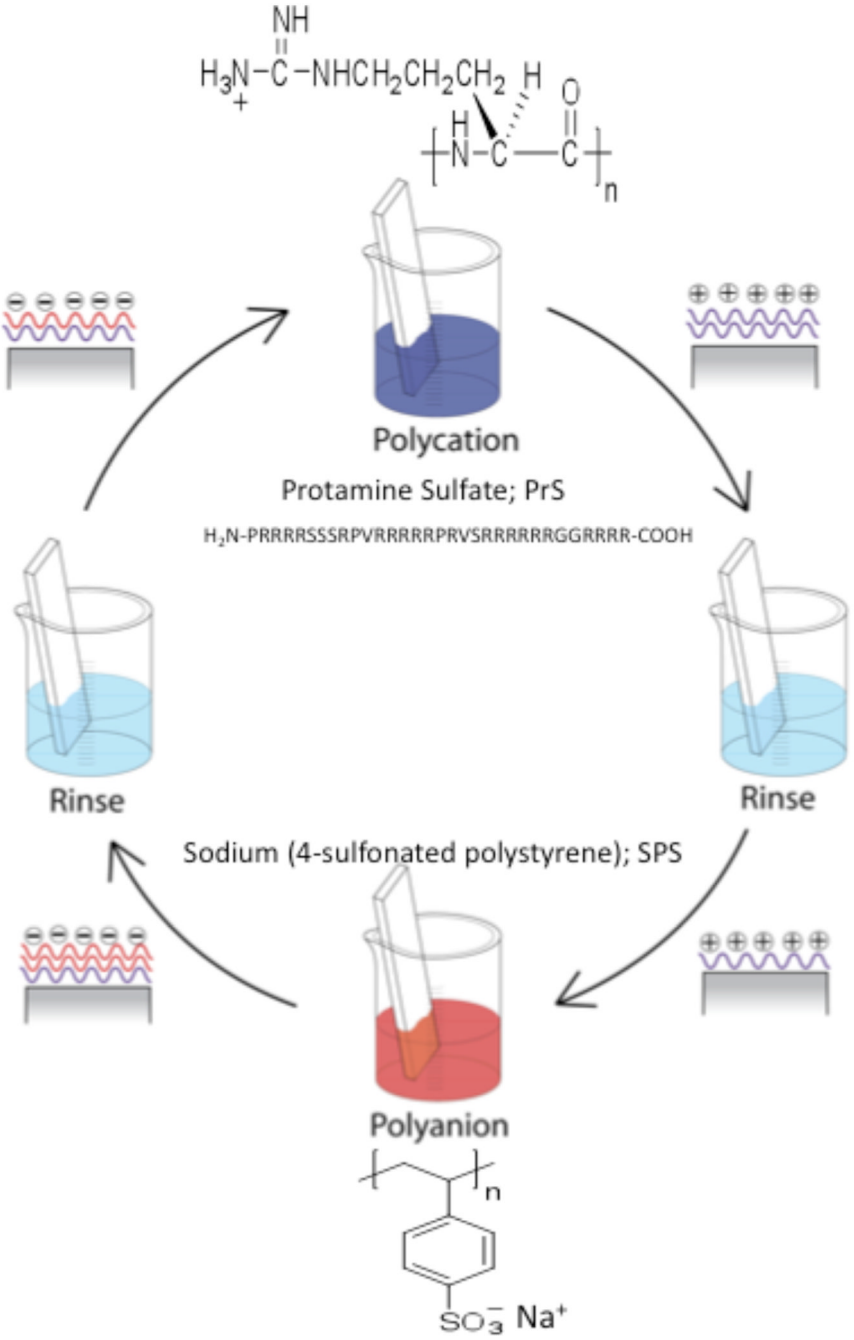

Figure 1. Layer-by-layer assembly of $(PrS/SPS)_n$ PEMs

Substrate is first submerged in the polycation solution, protamine sulfate (PrS); 21 of 32 amino acids are arginine, R. Following a rinse in deionized water, the PrS-coated substrate is then immersed in the polyanion solution, sodium (4-sulfonated poystyrene) (SPS), followed by another water rinse.

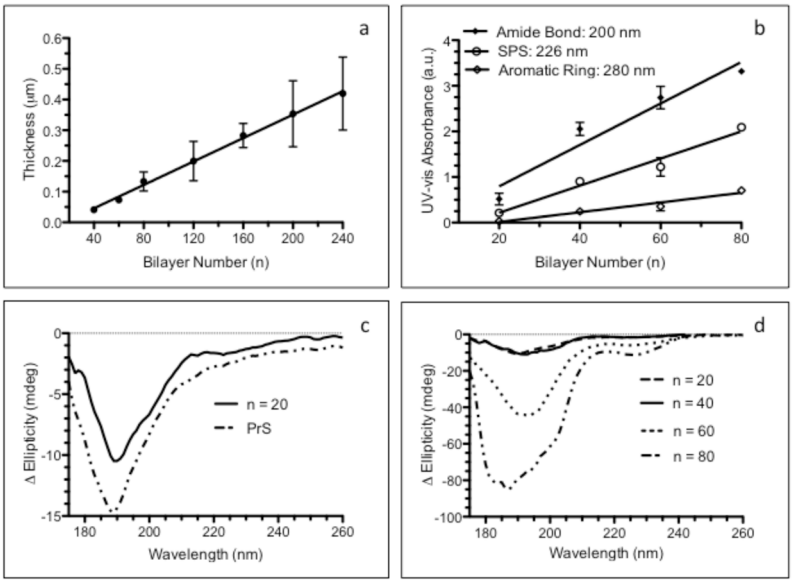

Figure 2. Characterization of dry $(PrS/SPS)_n$ PEM growth

(a) Profilometry measurements of dry film thickness. (b) UV-Vis spectroscopic analysis of $(PrS/SPS)_n$ PEMs functionalized quartz showing absorbance associated with the amide bonds (200 nm) and aromatic amino acid residues (280 nm) of PrS and the characteristic SPS absorbance at 226 nm. (c) CD spectra of PrS-coated and $(PrS/SPS)_{20}$ quartz. (d) CD spectra of dry $(PrS/SPS)_n$ PEM functionalized quartz.

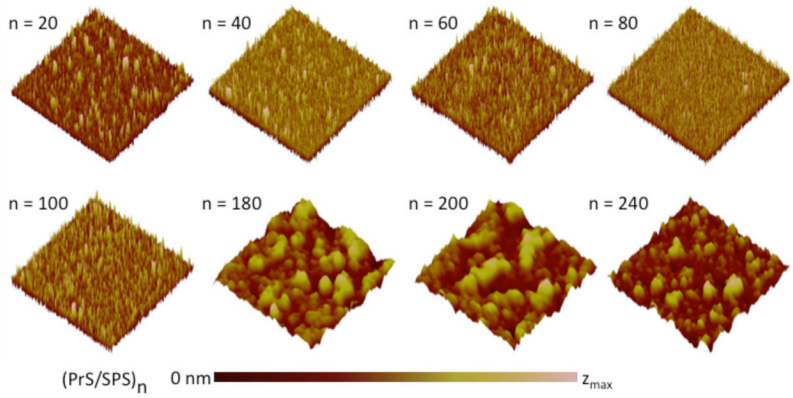

Figure 3. Surface morphology of $(PrS/SPS)_n$ PEMs surfaces

AFM images (10 μm × 10 μm area) showed variation in the nanoscale topography of the surface of dry $(PrS/SPS)_n$ PEMs at different thicknesses (z_{max} = 110 nm, 60 nm, 30 nm, 35 nm, 40 nm, 1500 nm, 1600 nm, and 1000 nm for n = 20, 40, 60, 80, 100, 180, 200, and 240, respectively).

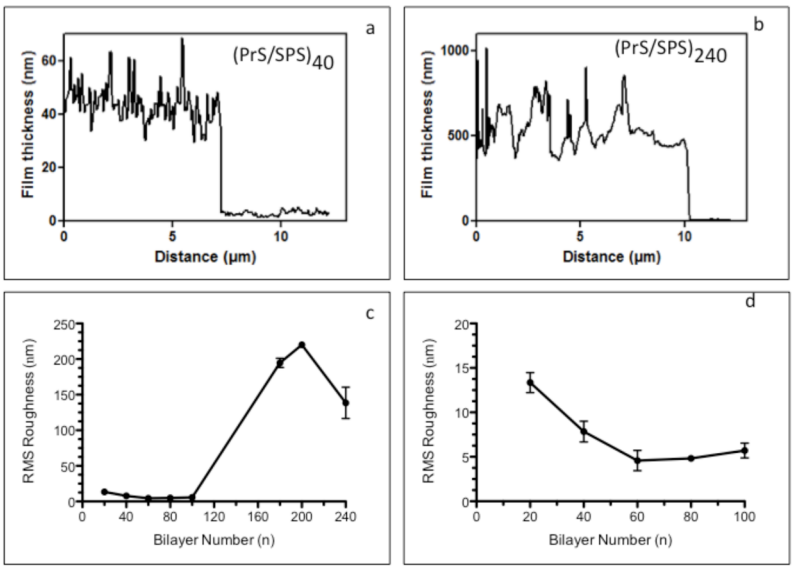

Figure 4. AFM scratch test and roughness of $(PrS/SPS)_n$ PEMs surfaces

AFM line scans (a and b) across the scratched $(PrS/SPS)_{40}$ and $(PrS/SPS)_{240}$ PEMs showed complete coverage of the substrate surface by the nanoscale thin films. (c) The RMS roughness values of the films were dependent on the thickness (bilayer number). (d) Magnification of lower *n* region of part b showing the decrease in RMS roughness as *n* increased from 20 to 100 bilayers.

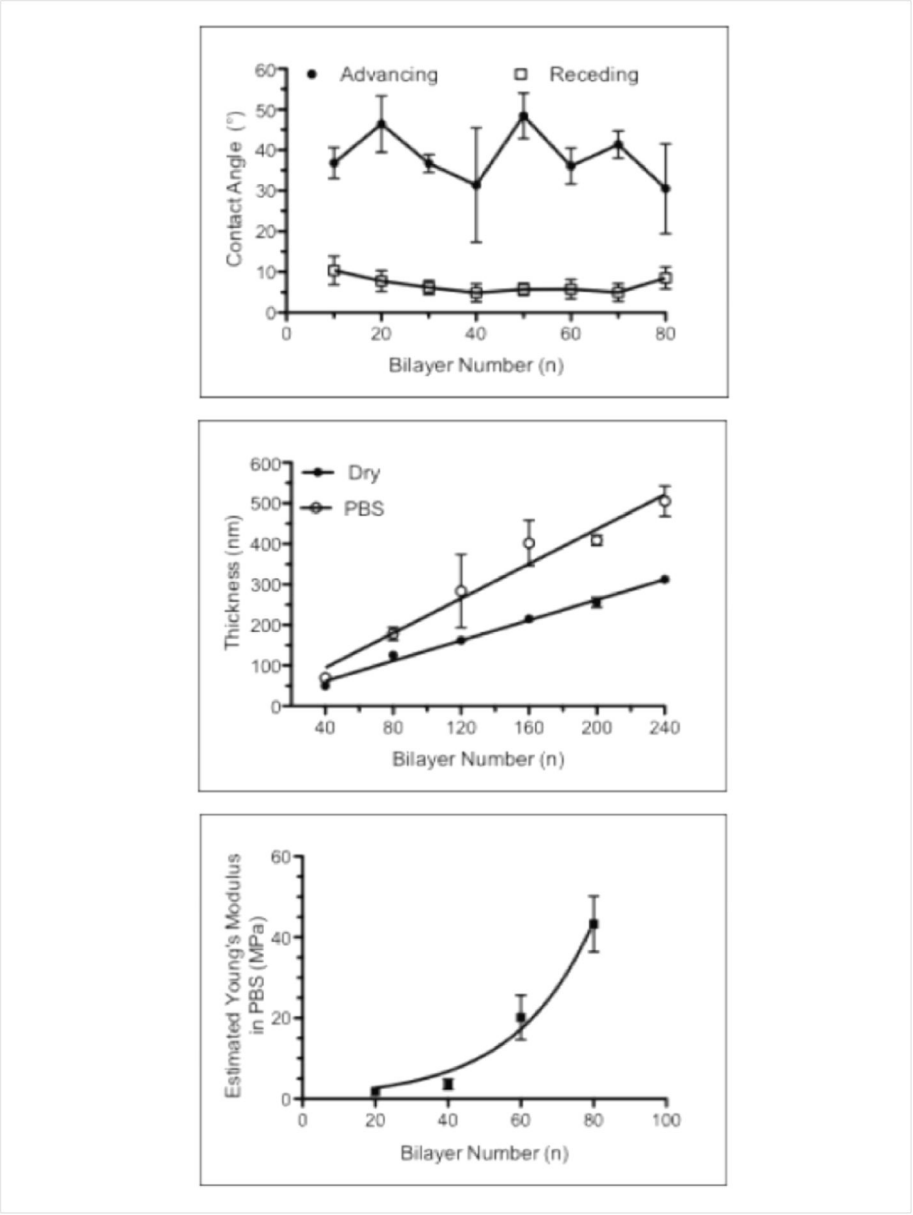

Figure 5. Liquid-phase chacterization of $(PS/SPS)_n$ PEMs

(a) Dynamic air-water contact angle measurements of $(PrS/SPS)_n$ PEMs. (b) In-situ spectroscopic ellipsometry thickness measurements of $(PrS/SPS)_n$ PEM functionalized silicon. (c) Liquid-phase AFM measurements of Young's moduli obtained from hydrated $(PrS/SPS)_n$ PEM functionalized silicon surfaces.

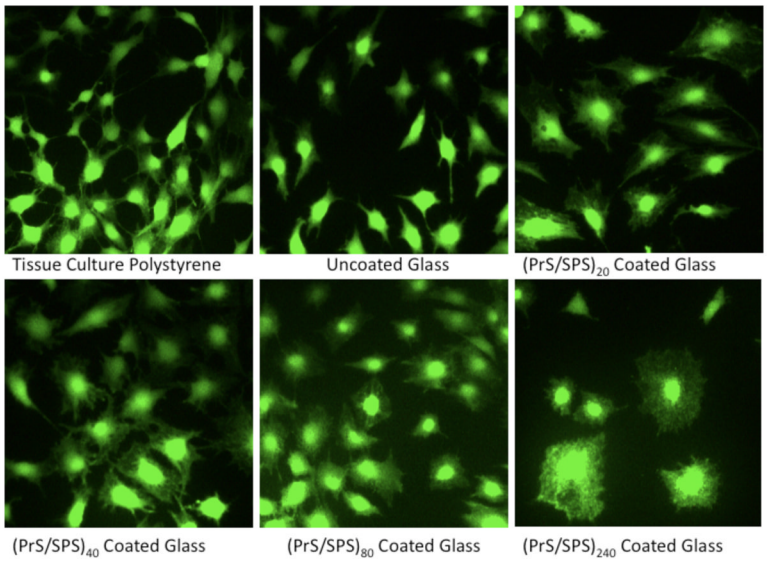

Figure 6. MC3T3-E1 morphology on conventional tissue culture substrates (TCPS and glass) and $(PrS/SPS)_n$ PEM coated glass surfaces in culture medium containing 10% FBS

Calcein deposits in the cytoplasm of MC3T3-E1 cells demonstrated alterations in cell morphology (cytoplasm area to total cell area ratio) and cytoplasm projections on PrS/SPS coated surfaces compared to TCPS and uncoated glass surface.

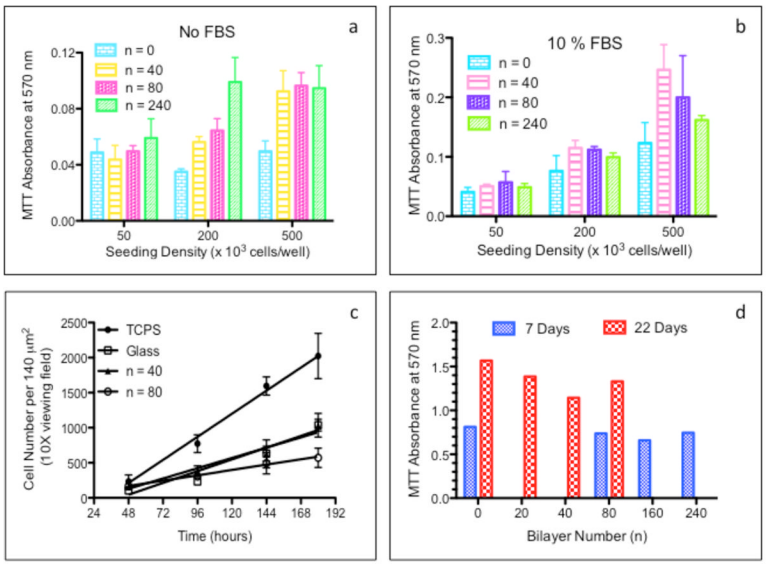

Figure 7. Adhesion and proliferation of MC3T3-E1 on PEMs in serum-free and serum-containing cultures

MC3T3-E1 adhesion to $(PrS/SPS)_n$ PEMs coated and uncoated glass surfaces in serum-free culture medium (a) and in culture medium containing 10% FBS (b). (c) MC3T3-E1 pre-osteoblast seeded at 5,000 cells/cm^2 onto $(PrS/SPS)_n$ functionalized glass surfaces and to control surfaces (TCPS and uncoated glass) proliferated in presence of 10% FBS. (d) Metabolic activity of MC3T3-E1 pre-osteoblasts seeded at high-density (50,000 cells/cm^2) on uncoated and $(PrS/SPS)_n$ functionalized glass surfaces were determined after 1 week and 3 weeks culture.

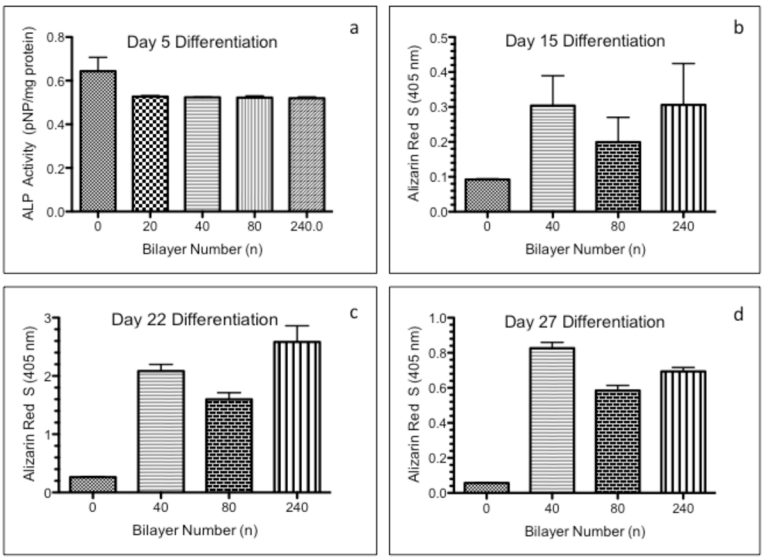

Figure 8. Osteogenic differentiation of MC3T3-E1 cells on $(PrS/SPS)_n$ PEMs

Differentiation of MC3T3-E1 cells seeded at high density (50,000 cells/cm^2) on uncoated and $(PrS/SPS)_n$ functionalized glass surfaces was quantified by alkaline phosphatase activity (ALP; a) and Alizarin Red S (ARS) at 15 days (b), 22 days (c), and 27 days (d) of culture in osteogenic media.

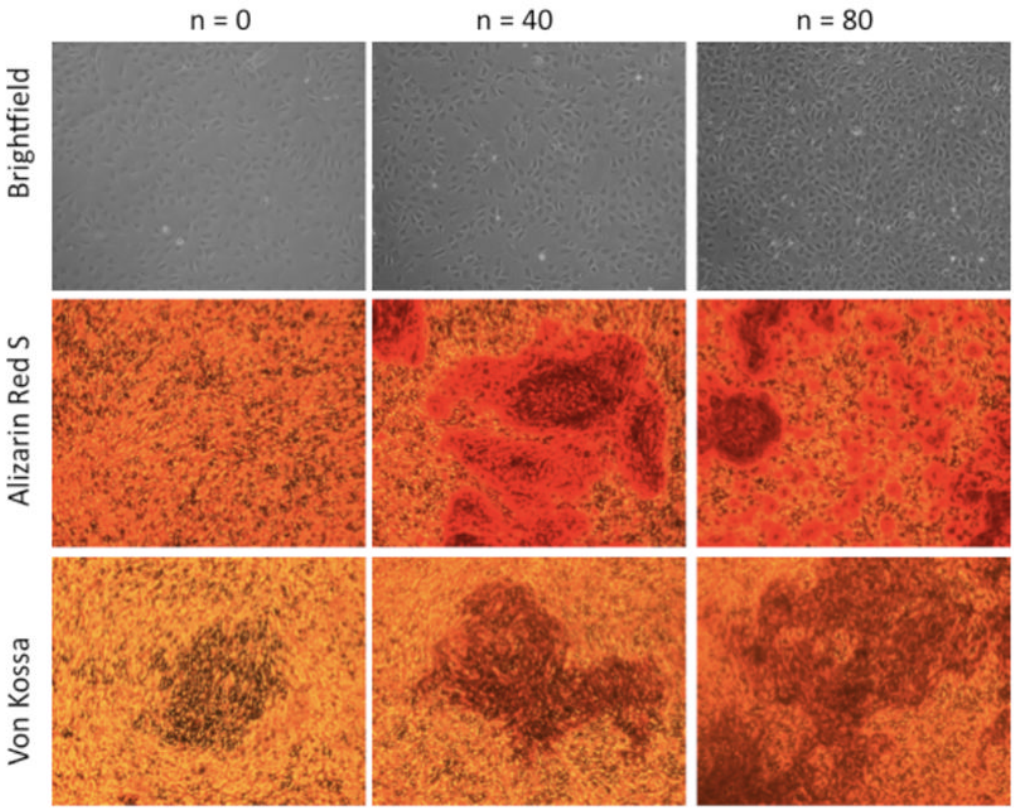

Figure 9. Long-term culture of MC3T3-E1 cells on $(PrS/SPS)_n$ PEMs

Micrographs of MC3T3-E1 cells on uncoated $(PrS/SPS)_0$, $(PrS/SPS)_{40}$, and $(PrS/SPS)_{80}$ during proliferation (brightfield) and differentiation (Alizarin Red S and von Kossa). All surfaces supported adhesion and proliferation of MC3T3-E1 cells to achieve near confluence prior to onset of osteogenic differentiation. Alizarin Red S staining demonstrated increased calcium deposits with increasing thickness of the PEMs. Von Kossa staining showed that mineralization of these calcium deposits was also dependent on the PEM thickness.